ROYAL SOCIETY
OF CHEMISTRY

PAPER

Check for updates

Valence band modification of Cr_2O_3 by Ni-doping: creating a high figure of merit p-type TCO†

Elisabetta Arca, [ID] ‡*[a] Aoife B. Kehoe,[b] Tim D. Veal, [ID] [c] Aleksey Shmeliov,[b] David O. Scanlon, [ID] [de] Clive Downing,[b] Dermot Daly,[b] Daragh Mullarkey,[a] Igor V. Shvets,[a] Valeria Nicolosi[b] and Graeme W. Watson [ID] [b]

p-Type transparent conductors and semiconductors still suffer from remarkably low performance compared to their more widespread n-type counterparts, despite extensive investigation into their development. In this contribution, we present a comparative study on the defect chemistry of potential p-type transparent conducting oxides Mg-doped and Ni-doped Cr_2O_3. Conductivities as high as 28 S cm^{-1} were achieved by Ni-doping. By benchmarking crystallography and spectroscopy characterization against density functional theory calculations, we show that the incorporation of Ni into Cr_2O_3 contributes to the composition of the valence band, making the formed holes more delocalized, while Mg states do not interact with the valence band in Mg-doped Cr_2O_3. Furthermore, it is experimentally proven that Ni has a higher solubility in Cr_2O_3 than Mg, at least in the highly non-thermodynamic deposition conditions used for these experiments, which directly translates into a higher acceptor concentration. The combination of these two effects means that Ni is a more effective acceptor in Cr_2O_3 than Mg and explains the improved conductivity observed for the former.

1 Introduction

Transparent conducting oxides (TCOs) are a particular class of materials which combine both optical transparency and electrical conductivity.[1–4] This peculiarity arises from the stringent dual requirements of having the first allowed optical transition at energy values higher than 3.1 eV and having uncompensated shallow donor (or acceptor) states close to the bottom (top) of the conduction band minimum (valence band maximum).[1–4] The transparency window in the visible range is normally realized by (i) having a material with a wide fundamental band gap, such as in the case of n-type $BaSnO_3$[5] or p-type $CuAlO_2$,[6] or (ii) having a smaller band gap associated with a forbidden optical transition and the first allowed optical transition higher than 3.1 eV, like in the case of n-type In_2O_3[7] or p-type SnO.[8] Dopability, either n- or

p-type, is achieved *via* alignment of the band edges of the oxides with respect to the vacuum level and, at the same time, the ability to insert uncompensated defects.[9–11]

To date, p-type transparent conductors and semiconductors have displayed severely poorer properties than their n-type counterparts. So far the best reported p-type TCOs have conductivities in the range of 10^2 S cm^{-1}, for example delafossite $CuCrO_2$:Mg (conductivity 220 S cm^{-1} with 30% transparency)[12] and layered cobaltate $Bi_2Sr_2Co_2O_y$ (conductivity 222 S cm^{-1} with 50% transparency).[13] More recently, Zhang *et al.*[14] have reported Sr-doped $LaCrO_3$ as a promising new p-type transparent conducting oxide, with $LaSr_{0.25}Cr_{0.75}O_3$ and $LaSr_{0.5}Cr_{0.5}O_3$ achieving conductivities of 15 S cm^{-1} and 54 S cm^{-1}, respectively, although it was noted that higher conductivities *via* increased dopant concentration can come at the expense of reduced transparency (54.2% and 42.3%, respectively). These values of conductivity are still two or three orders of magnitude lower than those achieved in n-type TCOs, such as ZnO:Al, In_2O_3:Sn or SnO_2:F, which are in the range of 10^4 S cm^{-1}.

The major shortcoming of p-type TCOs lies in their poor hole mobility. Despite the fact that high doping levels can be achieved,[15] the values of conductivity are inherently hindered by heavy effective masses[16,17] or by the highly localized nature of p and d states forming the valence band maximum (VBM), with the latter leading to polaronic conductivities.[18–21] Only a few p-type TCOs have shown mobilities reproducibly higher than 1 cm^2 V^{-1} s^{-1}, an example of which is SnO.[8,22,23]

[a] *School of Physics and CRANN, Trinity College Dublin, Dublin, Ireland.*
E-mail: earca@tcd.ie
[b] *School of Chemistry and CRANN, Trinity College Dublin, Dublin, Ireland*
[c] *Stephenson Institute for Renewable Energy and Department of Physics,*
School of Physical Sciences, University of Liverpool, Liverpool, L69 7ZF, UK
[d] *University College London, Kathleen Lonsdale Materials Chemistry,*
Department of Chemistry, 20 Gordon Street, London WC1H 0AJ, UK
[e] *Diamond Light Source Ltd., Diamond House, Harwell Science and Innovation*
Campus, Didcot, Oxfordshire OX11 0DE, UK
† Electronic supplementary information (ESI) available. See DOI: 10.1039/c7tc03545d
‡ Present address: National Renewable Energy Laboratory, 15013 Denver West Parkway, Golden, Colorado 80401, USA.

Overcoming these limitations has stimulated intense research activity in the field, from both an experimental and a theoretical point of view. $CuAlO_2$, the first reported p-type TCO,[24] overcomes the limitations of hole localisation on O ions by combining semiconductor Cu_2O with transparent insulator Al_2O_3 such that the Cu d states mix with the O p states in the valence band, promoting delocalization. Various materials were considered over the past two decades include delafossite structures,[21,25–31] oxychalcogenides,[32–35] spinel structures,[36–39] cobaltates,[13] more complex or exotic structures such as $KAg_{11}(VO_4)_4$[40] and recently, Ha *et al.* have expanded the concept of Sn(II)-based oxide as suitable materials to achieve low effective mass p-type TCOs.[41]

Recently, we demonstrated the possibility of Cr_2O_3 as p-type transparent semiconductor oxide, by doping it with Mg to improve its electrical conductivity and retain the transparency properties by introducing an ammonium precursor in the solution.[42,43] Lately, Cr_2O_3 has received considerable attention as a p-type transparent conductor,[43–47] with a few reports also discussing the possibility of n-type behavior in Cr_2O_3 by doping it with Ti.[48–51] While Mg is a popular choice in the literature as a hole dopant for Cr_2O_3,[46,52,53] further improvement can be achieved if shallower acceptors than Mg are used. To this end, Ni has been considered,[53,54] with the highest conductivity of 5 S cm^{-1} recently achieved by Arca *et al.*[45]

In this contribution, we compare the effect of p-type dopants Mg and Ni in epitaxial Cr_2O_3 films. We show that Ni is a far more effective dopant than Mg, achieving conductivities an order of magnitude higher. Moreover, through a combination of crystallography, spectroscopy and density functional theory (DFT) calculations, we attempt to establish the origin of the improved conductivities and in particular the role of Ni as a more effective acceptor than Mg.

2 Experimental details

Cr_2O_3 films were deposited on a single side polished sapphire (c-Al_2O_3, (0001)-oriented) mono crystalline substrate using a pulsed laser deposition chamber (SURFACE) operating at a base pressure of 5×10^{-7} bar. A KrF laser (λ = 248 nm) was used at a repetition rate of 10 Hz. The laser density on the target was adjusted to be 0.8 J cm^{-2}. Ni-Doped, Mg-doped and an undoped target were prepared by solid state reaction. Details of the target preparation are reported elsewhere.[45,46] For the deposition, different combinations of temperature and pressure were tested. Highest conductivity, while still preserving phase purity, were found using deposition temperature of 773 °C and 923 °C for Ni-doping and Mg-doping, respectively, and optimum deposition pressure of 1×10^{-4} bar for both dopants. For both target and thin films, the composition is expressed based on the cation ratio, *i.e.* the ratio $M_{at}/(M_{at} + Cr_{at})$ where M is either Mg or Ni. After each deposition, films were subjected to structural characterization to verify the purity of the phase deposited. To this end, High Resolution X-ray Diffraction (HRXRD) was performed using a Bruker D8 Discover. The thickness of each

individual sample was determined by X-Ray Reflectivity (XRR). The effect of doping on the electronic properties of the films was determined by X-ray Photoelectron Spectroscopy (XPS) using an Omicron Multi-Probe XPS equipped with a monochromated Al Kα X-ray source in conjunction with an Omicron EA 125 hemispherical analyser. A pass energy of 20 eV was used, which combined with detector and source resolutions, brings the resolution up to 0.5 eV. For undoped, insulating samples, an Omicron CN 10 charge neutralizer was used during XPS acquisition. Beam energy, emission current, and deflection were optimized to achieve a Full Width at Half Maximum (FWHM) of the O 1s peak comparable to the line-width typical of samples not affected by charging (FWHM = 1.2 eV). Samples were loaded into the XPS chamber immediately after deposition to minimize contamination by exposure to atmospheric gases. We realigned all the spectra so that the signal of the aliphatic C 1s core-level meets the standard value of 285 eV. The realignment was only of about 0.2 eV for all conductive samples, and for some of them, it was not even necessary as the signal of adventitious C was already coincident with a binding energy of 285 eV. Electrical characterization was performed in a 4 point probe apparatus using a linear configuration and computer controlled Keithley 2400 source meter. Conductivity values were calculated based on the sheet resistance and thickness measurements as determined by XRR. Additional microstructural and compositional characterization was performed by Transmission Electron Microscopy (TEM). Lamellae were prepared using a gallium based Focused Ion Beam system (Carl Zeiss Auriga 40). A lamella was milled in the region of interest and was then placed on a TEM grid using the *in situ* lift out technique. The lifted out lamella was subsequently thinned to $\sim$150 nm with a 15 kV at 200 pA ion beam and then polished to $\sim$50 nm in the region of interest with a 5 kV at 20 pA ion beam. High-resolution TEM (HRTEM) images were acquired using a FEI Titan operated at 300 keV. Atomically resolved annular dark-field (ADF) scanning TEM (STEM) images were obtained using Nion UltraSTEM operated at 200 keV with collection angles of 99–200 mrad. Energy dispersive X-ray (EDX) maps were acquired using a Bruker 100 mm^2 windowless EDX available in the Nion UltraSTEM.

3 Computational details

All DFT calculations were carried out using the VASP package,[55–57] which models crystalline systems by using periodic boundary conditions and expanding crystal wave functions in terms of a plane wave basis set. Interactions between the core states (represented by atomic functions) and valence electrons (described by plane waves) are modelled using the projector augmented wave (PAW) method, with the cores defined here as Cr:[Ar], O:[He], Mg:[Be], and Ni:[Mg]. The PBE functional was used to describe exchange and correlation,[58] with $+U$ values[59] to combat self-interaction error applied to the Cr 3d states, due to the highly localized nature of d states, and to the O 2p states, due to the importance of accurately modelling the typically O 2p dominated valence band of p-type oxides. U values of 3 eV and

This journal is © The Royal Society of Chemistry 2017

J. Mater. Chem. C, 2017, **5**, 12610–12618 | **12611**

5 eV, respectively, were derived from comparison to XPS spectra to best reproduce valence band shape and features as outlined in our previous study on Mg-doped Cr_2O_3.[46] A U of 5.3 eV was also applied to the Ni d states, a value which has been widely used in the literature to model Ni oxide systems with PBE.[60,61] A k-point mesh of Γ-centred $2 \times 2 \times 1$, a plane wave cut-off of 400 eV, and a force convergence criterion of 0.01 eV Å^{-1} were used to model the 120 atom $2 \times 2 \times 1$ expansion of the 30 atom hexagonal unit cell. The formation energy ($E_f(D,q)$) of a defect (D) in each of its possible charge states (q) was calculated according to eqn (1).

$$\Delta E_f(D, q) = \left(E^{D,q} - E^P \right) + \sum_i n_i(E_i + \mu_i) + q\left(E_{\text{Fermi}} + \varepsilon_{\text{VBM}}^P\right) + E_{\text{align}} \tag{1}$$

The first term, $E^{D,q} - E^P$, is the difference in energy between the defective and pure systems. In the second term, n_i is the number of atoms of type i taken from or added to an external reservoir, as a function of both the elemental reference energies calculated from their standard states (E_i) and chemical potentials to represent the equilibrium growth conditions (μ_i). The chemical potentials are found with reference to the PBE + U calculated formation energy of pure Cr_2O_3, -12.54 eV. The formation energies of CrO and CrO_2 were also calculated to determine if they are competing phases under O-poor or O-rich conditions, respectively, but this was found not to be the case. The O-rich chemical potential limits were thus calculated to be $\mu_{\text{Cr}} = -6.27$ eV and $\mu_{\text{O}} = 0$ eV, and the O-poor limits are $\mu_{\text{Cr}} = 0$ eV and $\mu_{\text{O}} = -4.18$ eV. For the doped systems, μ_{Mg} and μ_{Ni} were calculated using the formation energies of their parent oxides MgO and NiO, resulting in $\mu_{\text{Mg}} = 3.53$ eV and $\mu_{\text{Ni}} = -2.94$ eV under O-rich conditions and $\mu_{\text{Mg}} = 0$ eV and $\mu_{\text{Ni}} = 0$ eV in the O-poor regime.

The third term in eqn (1) includes the charge state of the defect and is dependent on the electron chemical potential (E_{Fermi}) and the VBM eigenvalue of the pure system. Finally, E_{align} aligns the electrostatic potential between the pure and defective systems and corrects for finite-size effects in charged defect calculations,[62] with a value of 12.6 used for the dielectric constant based on the average of the experimentally reported values of 13.0 parallel to the a axis and 11.8 parallel to the c axis.[63] The thermodynamic transition levels of each defect are also calculated as in eqn (2), defined as the Fermi level at which different charge states q and q' of a particular defect have the same formation energy.

$$\varepsilon_D(q/q') = \frac{\Delta E_f(D, q) - \Delta E_f(D, q')}{q' - q} \tag{2}$$

All calculations were spin polarized. The magnetic moment of each atom in the initial configuration, as well as the overall difference between spin up and down components in the final configuration, was set for all calculations. For all defects, all plausible alternative spin orderings were considered, with the lowest energy configurations used in the final transition levels diagram.

4 Results

A target with a Ni cationic content of 7 at% was prepared, with phase pure films achieved at a deposition temperature of 773 K. This temperature was chosen as spurious peaks were present in the XRD pattern at any other deposition temperature tested (823 K, 873 K and 923 K), as shown in Fig. 1. These peaks, resulting from the formation of competing phases such as $NiCrO_4$ and NiO, were not observed at any value of temperature tested over the range 773 K to 873 K in our previous investigation using 5 at% Ni-doped targets.[45] All data on Mg-doped Cr_2O_3 presented herein is based on a target with a Cr : Mg ratio of 94 : 6, the concentration with which the best conductivities were achieved in our previous work.[46] These concentrations were found to be those at which no spurious phase were formed, and thus were taken to be the highest value of dopant that, experimentally, could be inserted in the material. The lack of spurious phase as determined by the XRD or TEM analysis was determined to be the solubility limit for both dopants.

HRXRD patterns of both Ni-doped and Mg-doped Cr_2O_3 are reported in Fig. 2. Rocking curve measurements around the main Cr_2O_3 (006) reflection were performed to assess the defect density in both films. As shown in the inset in Fig. 2, the line-shape can be reconstructed by using two Gaussian components. Similar to previous literature reports,[64,65] the broader component is attributed to a higher density of defects in the interface region between the substrate and the heteroepitaxial films, whereas the second sharper component is relative to the over-layer, whose density of defects is notably reduced. This is common to both the Mg- and Ni-doped films, and the relative full width at half maximum (FWHM) are comparable: the sharper and broader components for Mg-doped films have FWHM of 86 arcsec and 972 arcsec, respectively, while the same components for Ni-doped films have values of 93 arcsec and 540 arcsec, respectively. The values of FWHM of the sharpest component are thus comparable, which means that the density of structural defects is similar.
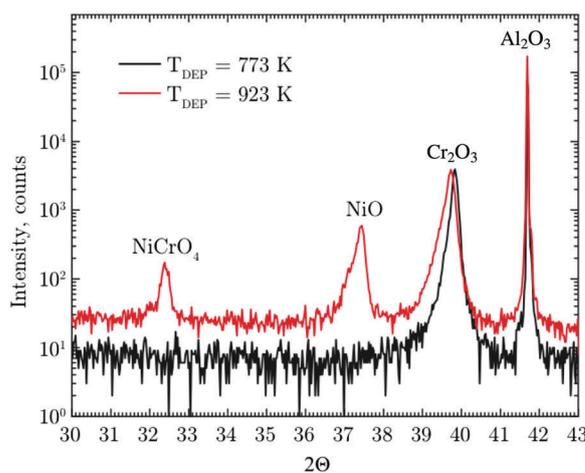

Fig. 1 XRD pattern of Ni-doped films grown out of the 7 at% target at 773 K (black) and 923 K (red). Samples grown at 823 K and 873 K show a very similar pattern to that recorded for the films deposited at 923 K.
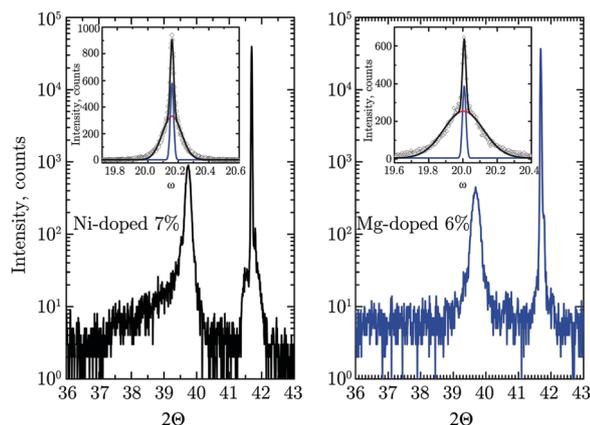
12612 | J. Mater. Chem. C, 2017, 5, 12610–12618

This journal is © The Royal Society of Chemistry 2017

Fig. 2 HRXRD of Ni-doped and Mg-doped Cr_2O_3 films.

A decrease in the value of the *c* parameter is observed in both the case of Ni- (13.596 Å) and Mg-doping (13.614 Å) relative to the undoped films (13.650 Å). This shift may appear counterintuitive: while ionic radii can vary substantially depending on the coordination number, for a substitutional type of impurity and a coordination number of 6, both Mg(II) (86 pm) and Ni(II) (83 pm) are expected to have a higher ionic radius than Cr(III) (75.5 pm).[66] This contraction of the crystallographic cell despite inserting ions of a higher ionic radii has been previously observed in the literature, for example for $Cu_{2-2x}Zn_xO$.[67] The quality of both Ni- and Mg-doped samples was further analyzed by HRTEM and atomically resolved ADF STEM to assess if nanoclusters of spurious phases were present. The total area examined for Ni- and Mg doped-lamellae is approximately 700 nm × 70 nm and 700 nm × 40 nm, respectively. Two large area images are shown in the Supplementary information 1 and 2 (ESI†). Additionally, the crystal structure of Cr_2O_3 and two representative images of Ni-doped Cr_2O_3 obtained from ADF STEM are shown in Fig. 3. No spurious phases have been detected, and only rare defective regions where interstitial atoms are clearly visible, have been observed for Ni doped films (Fig. 3(c)). Similar results were observed for the Mg-doped sample, albeit without interstitial defects, as shown in the Fig. S3 (ESI†). HRTEM images (Supplementary information 4 and 5, ESI†)

confirmed the absence of spurious phases. Notably, forbidden reflections are present in the Fast Fourier Transforms (FFT) of the HRTEM images. Their presence can be attributed to both dynamical scattering effects and the substitution of Ni or Mg on a Cr site. These results further support the conclusions drawn according the XRD analysis, confirming the absence of spurious phases even below the detection limit of the high resolution diffractometer used for this study.

The EDX mapping of the Ni and Mg distribution over a wide region, along with the corresponding ADF STEM images, is shown in Fig. 4. As can be seen, Ni and Mg atoms are not homogeneously distributed, and there are regions where the dopant tends to accumulate (such as Region 1 and 2 in respectively subfigure (c) and (d) of Fig. 4) and regions that are poorer in Ni and Mg content (Region 2 and 1 in each subfigure of Fig. 4). Ni concentration in these two regions was found by EDX to be 16 at% and 11 at%, respectively. Mg concentration in
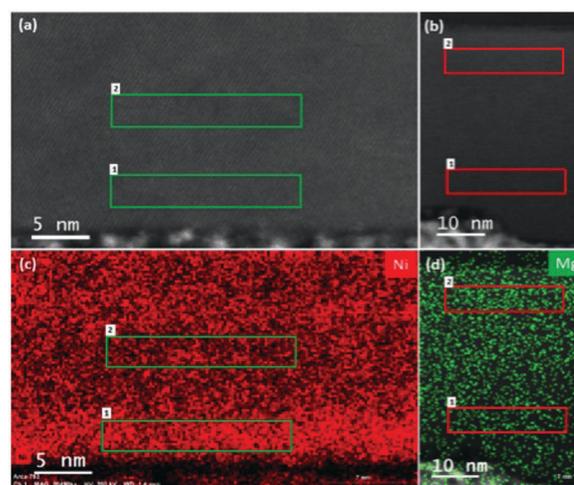

Fig. 4 ADF STEM images of (a) Ni-doped and (b) Mg-doped Cr_2O_3 with corresponding EDX maps in (c) and (d), respectively, showing the variation in the Ni and Mg concentration across the sample. Regions marked 1 and 2 show areas of increased and decreased dopant concentration, respectively. Pt deposited on the surface of Cr_2O_3 during lamellae preparation can be seen at the bottom of the images.
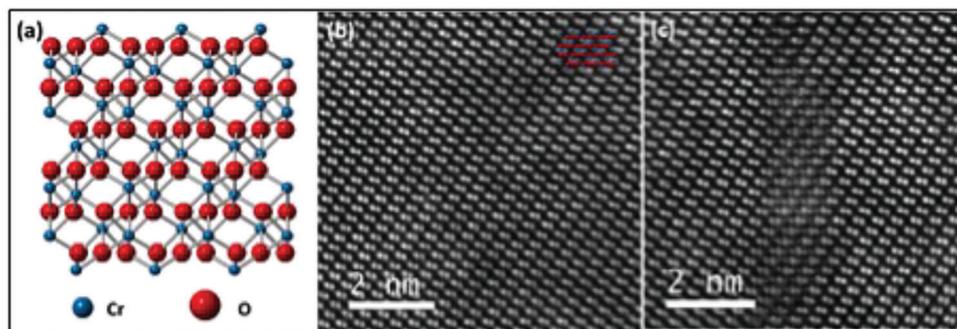

Fig. 3 (a) Structure of Cr_2O_3 along [100] direction, with Cr and O atoms shown in blue and red, respectively. (b) and (c) ADF STEM images of Ni doped Cr_2O_3 lamella showing respectively a region without any crystallographic defect and a region with interstitial atoms. Only Cr columns are visible in the images due to the strong Z-contrast.

This journal is © The Royal Society of Chemistry 2017

J. Mater. Chem. C, 2017, **5**, 12610–12618 | **12613**

Regions 1 and 2 was found to be 6.6 at% and 4.9 at%, respectively. DFT calculations for a 12.5 at% Ni-doped and a 8.3 at% Mg-doped system were performed, in which it was found that it is energetically preferential to place all of the dopants adjacent to one another in clusters instead of being homogeneously distributed throughout the supercell, corroborating the inhomogeneous distributions of Ni and Mg experimentally found throughout the films. Notably, the EDX determined concentration of incorporated Mg is considerably lower than that of Ni despite their similar target compositions. Conductivity measurements were carried out on a large number of films prepared from the 7 at% Ni target. Most samples were measured to have conductivities of around 20 S cm^{-1}, with the best samples reaching 28 S cm^{-1}. This is in comparison to the 5 ± 1 S cm^{-1} previously measured for samples produced from a 5% Ni-doped target[45] and the 1 ± 0.1 S cm^{-1} obtained from the 6 at% Mg target, the highest conductivity achieved for Mg-doped films over a range of tested Mg concentrations in our previous work.[46]

This therefore shows both that the higher Ni-doping concentration is conducive to better conductivity and that Ni-doping of Cr_2O_3 results in an improvement in electronic conductivity of more than an order of magnitude over Mg-doping. Notably, the conductivity of samples prepared with the 7 at% Ni target decreases significantly with increasing deposition temperature as competing phases are formed, as seen from Fig. 5 (top panel). The improvement in conductivity of Ni-doping *versus* Mg-doping is directly correlated to the lower activation energy observed for Ni-doping (70 meV as determined from the Arrhenius plot shown in Fig. 5 (bottom panel)) in comparison to the Mg-doping (170 meV). While the XRD pattern of the Ni doped samples having 20 S cm^{-1} shown in Fig. 1 are symmetric, the sample having 28 S cm^{-1} show a non-perfectly symmetric peak. Variations in Ni concentrations together with small defective regions, as identified by TEM and EDX, are most likely the cause for the asymmetry in the XRD peak associated with this highly conductive sample, yet their presence seems to be non-deleterious for the electrical properties, as noted by the high conductivities of the films.

The optical properties of the Ni-doped films having conductivity equal or higher than 20 S cm^{-1} are shown in Fig. 6. Transmittance for Ni-doped films ranges from 55% to 35% across the visible range, with an average value of 40%. These values are comparable to those previously reported for Mg-doped samples[46] (from 52% to 40% across the visible spectra). A major limitation to transmittance is the reflectance loss due to the large difference between the refractive index of both air and sapphire in comparison to Cr_2O_3, which is equal or higher than 20% across the entire spectral range.

Using DFT, the transition levels of a Mg ion on a Cr site, a Mg interstitial ion, a Ni ion on a Cr site, and a Ni interstitial ion were calculated, as shown in Fig. 7. Multiple interstitial positions were tested, but the only location in which the dopant relaxed was the "vacant" cation site in the corundum structure, in which one third of the octahedral sites on the cation sublattice are unfilled. Defect formation energies were calculated under both O-rich/Cr-poor and O-poor/Cr-rich conditions
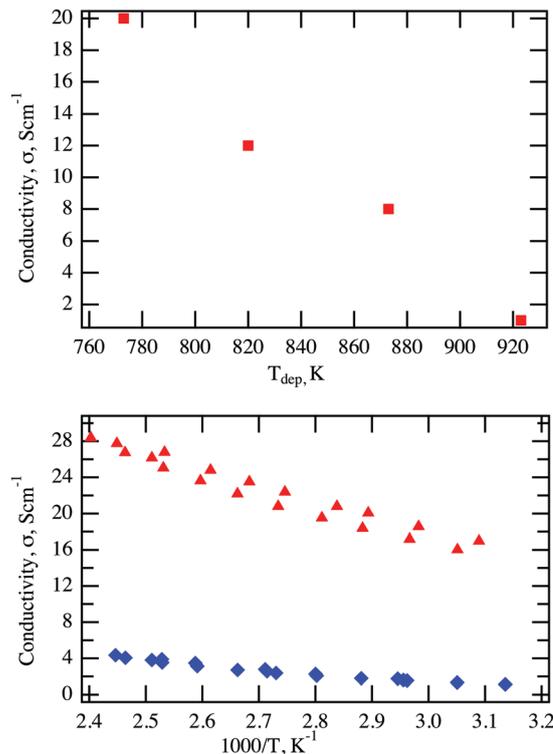

Fig. 5 (top panel) The conductivity of Ni-doped Cr_2O_3 prepared with a 7% Ni target as a function of deposition temperature and (bottom panel) comparison between the Arrhenius plot of a Ni-doped (red triangles) and a Mg-doped (blue diamonds) Cr_2O_3 thin films.
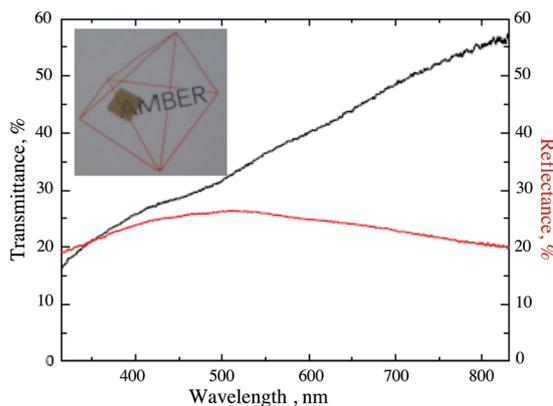

Fig. 6 Visible transmittance (black line) and reflectance (red line) of a Ni-doped sample.

using chemical potential limits as outlined above. The intrinsic defects with the lowest formation energy (O peroxide species in the O-rich regime and O vacancy in the O-poor) and the most shallow ionisation level (Cr vacancy and Cr interstitial for O-rich and O-poor conditions, respectively), as calculated in our previous work,[46] are shown for comparison.

In the O-rich regime, the Mg ion on a Cr site has a neutral state formation energy of 0.66 eV and a relatively shallow (for a p-type defect) $0/-1$ transition level of 0.42 eV. The Ni substitutional ion has a formation energy and first ionisation level of
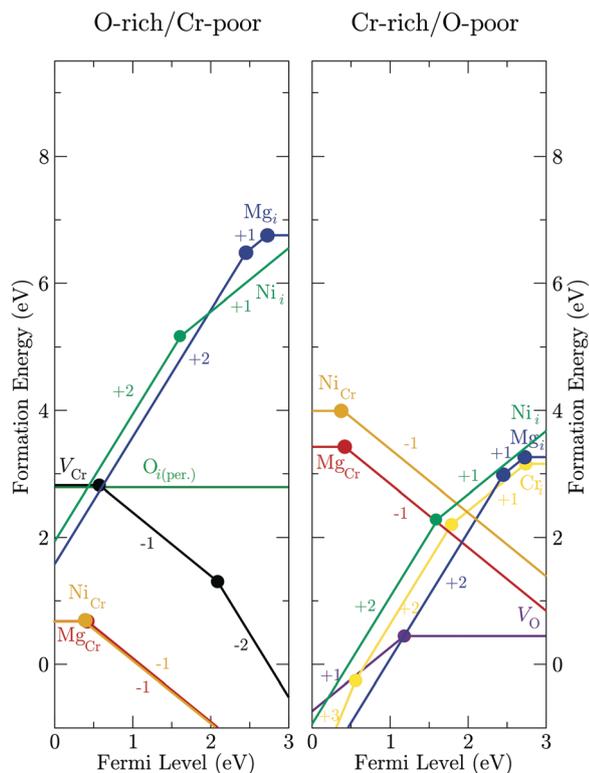
12614 | *J. Mater. Chem. C*, 2017, **5**, 12610–12618

This journal is © The Royal Society of Chemistry 2017

Fig. 7 Transition levels diagrams of Mg and Ni interstitial and substitutional ions in Cr_2O_3, under both O-rich and O-poor conditions.

0.67 eV and 0.40 eV, respectively. Notably, these values are very similar for both dopants. The n-type Mg interstitial and Ni interstitial have formation energies of 6.78 eV and 6.53 eV, respectively, far higher than the p-type substitution defects. The Mg and Ni dopant ions are therefore uncompensated across the span of the band gap, resulting in the experimentally observed p-type conductivity under O-rich conditions.

Under O-poor conditions, where n-type defects should be more favorable, the n-type Mg interstitial has a formation energy and a first ionisation level of 3.25 eV and 0.23 eV, respectively. Mg on a Cr site has a formation energy of 3.42 eV and a first ionisation level of 0.42 eV. An interesting effect of Mg-doping under O-poor conditions is that these two Mg related defects in Cr_2O_3 intersect on the transition level diagram, which would result in the Fermi level being trapped at 1.92 eV. Therefore, neither n- or p-type conductivity would be expected to be observed when the material is grown in an O-poor environment. A similar situation is observed for Ni-doped Cr_2O_3 under O poor conditions. Ni on a Cr site has a formation energy of 4.00 eV and a first ionisation level of 0.40 eV. The Ni interstitial has its first transition in the conduction band (1.00 eV above the conduction band minimum), which would be advantageous for n-type conductivity were it not for the fact that the formation energy is prohibitively high at 4.59 eV. As with the Mg-doped system under O-poor conditions, the Fermi level is pinned mid-gap, in this case between the Ni on a Cr site and the Cr interstitial, at an energy of 1.99 eV. As such, for both Mg- and Ni-doping of Cr_2O_3, electronic conductivity is unlikely to occur when the materials

are deposited under O-poor conditions, and only p-type conductivity should be observed in an O-rich regime.

The effect of Ni-doping on the electronic properties of Cr_2O_3 was assessed by XPS. As XPS is a surface sensitive technique, the stoichiometry of the surface needs to be determined in order to assess if the XPS determined density of states are a good representation of the material's bulk properties. The Ni concentration at the surface was determined by deconvolution of the Cr 3s and Ni 3p peaks as shown in Fig. 8 for the films grown using 5 at% and 7 at% doped targets. These were then compared to the bulk values as determined by EDX spectroscopy. The Cr 3s and Ni 3p photoelectrons were chosen as they have similar binding energies and approximately the same inelastic mean free path (IMFP) of $\lambda = \sim 3$ nm. Details on how to calculate the IMFP are reported in the ESI.† According to the Beer–Lambert law, 95% of the XPS signal is from $3\lambda = 9$ nm. Curve fitting Cr 3s and Ni 3p regions is complicated by the presence of satellite features associated with the well-known shake-up satellite peaks at higher binding energy than the main peaks. These features are consistent with previous reports for Cr_2O_3 and NiO and have been fitted in order to be included in determining the total Cr 3s and Ni 3p peak areas and applying the relative sensitivity factors for composition determination.

The surface concentration of Ni, as determined by the proportion of the cation sublattice was found to be 10 at% and 12 at% (± 2 at%) for films grown out using the 5 at% and 7 at% doped targets respectively. The surface concentration found in the films is in good agreement with the bulk determined concentration, which was found to be 13 at% and 14 at%, respectively (± 2 at%). Details of the fitting procedures and the parameters used to determine the surface composition, are reported in the ESI,† Tables SI and SII. The VBM for both Mg-doped and Ni-doped films were recorded and compared (Supplementary information 6, ESI†). The increased conductivity of the Ni-doped films is mirrored by a downwards shift of the Fermi level towards the valence band (VB) edge, which was found to be 0.2 eV above the VBM for both the 10 at% and 12 at% doped films[45] (Supplementary information 6, ESI†). For comparison, the
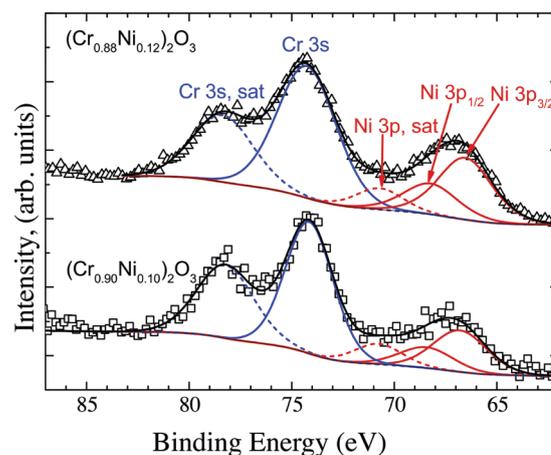

Fig. 8 Deconvolution of the Cr 3s and Ni 3p peaks to determine the concentration of Ni at the surface.

This journal is © The Royal Society of Chemistry 2017
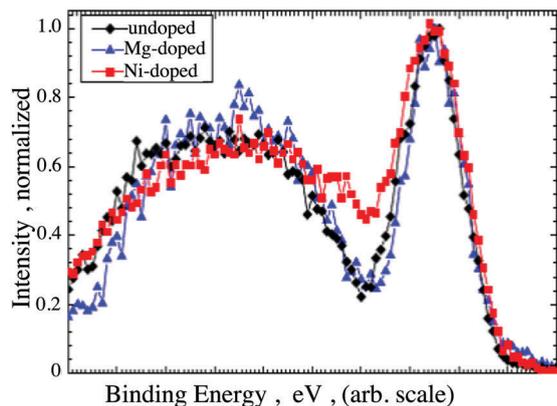
J. Mater. Chem. C, 2017, **5**, 12610–12618 | **12615**

Fig. 9 Comparison between the VB shape of an undoped, Mg-doped and Ni-doped Cr_2O_3 films. The graphs are shifted in order highlight the change in shape upon Ni-doping.

undoped films have a Fermi level placed roughly 1 eV above the VB edge, whereas Mg induces a downwards shift of the Fermi level to 0.5 eV above the VB edge.[46] In addition, doping with Ni results in a noticeable modification of the overall shape of the VB. In order to highlight the differences, the VB shapes of undoped, Mg- and Ni- doped films were shifted to superimpose with one another as seen in Fig. 9. Notably, the VB shapes of undoped and Mg-doped films are identical whereas the region of low density normally present between the Cr 3d and O 2p states is considerably less pronounced in the case of Ni doped films.

The electronic density of states (EDOS) were generated with DFT to examine the influence of Ni and Mg on the VB. The total and partial EDOS of undoped, Mg-doped, and Ni-doped Cr_2O_3 are shown in Fig. 10. Notably, there is no interaction of the valence Mg s states with the VB of the host system as they are significantly lower in energy, while in the Ni-doped system, the Ni d states are present in the VB where they can mix with the O 2p states. This is in good agreement with the experimentally obtained XPS data, as the Ni 3d states occupy the energetic range of zero density observed in the Mg-doped system between 1 eV and 2 eV.
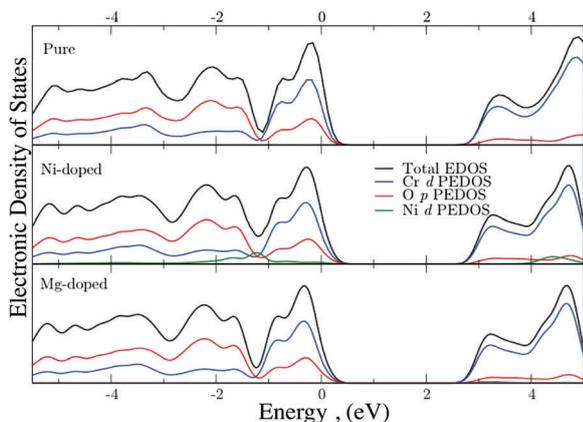

Fig. 10 Total and partial EDOS of (a) undoped, (b) Ni-doped and (c) Mg-doped Cr_2O_3. The top of the VB is aligned to 0 eV in all cases.

5 Discussion

Experimentally, it was demonstrated that Ni incorporation in Cr_2O_3 produces films with considerably higher conductivities than Mg-doped films, achieving values of 28 S cm^{-1}, which is higher than any Cr_2O_3 doped films previously reported in the literature. TCOs are often assessed using a ratio of electrical conductivity to visible absorption coefficient known as the figure of merit, calculated from the sheet resistance, total visible transmission, and total visible reflectance.[68] The figure of merit determined here for Ni-doped Cr_2O_3 is 110 MΩ^{-1}. For comparison, the best n-type materials typically have values on the order of 1 Ω^{-1}, while other prospective p-type materials such as $CuCrO_2$:Mg, $Bi_2Sr_2Co_2O_y$, $LaSr_{0.25}Cr_{0.75}O_3$ and $LaSr_{0.5}Cr_{0.5}O_3$ have figures of merit of 4600 MΩ^{-1},[12] 800 MΩ^{-1},[13] 196 MΩ^{-1},[14] and 314 MΩ^{-1},[14] respectively. Indeed, $LaSr_{0.25}Cr_{0.75}O_3$, despite not having the highest figure of merit, was recently claimed as the best p-type TCO based on the compromise between optical transparency and electrical conductivity.

To explain the improved conductivity of Ni-doped samples over Mg-doping, electrical measurements, structural characterization, spectroscopic measurements, and DFT calculations were performed. DFT calculations of the EDOS and experimentally determined XPS show a contribution of the Ni d-levels to the valence band, whereas Mg electronic levels do not contribute to it. The presence of Ni d-levels helps the delocalization of the formed holes, thus reducing the hole effective mass. The importance of a second cation in the formation of the VB and on the delocalization of the holes has been already proven for the case of $CuCrO_2$, where the effect is even more pronounced. Similar to the combination of Cu_2O's conductivity and the transparency of Cr_2O_3 in delafossite p-type TCO $CuCrO_2$, we propose that combining transparent insulator Cr_2O_3 with semiconductor NiO can result in mixing of their valence bands to produce a viable p-type TCO, something that MgO, itself an insulator, cannot achieve when mixed with Cr_2O_3.

In the case of the Ni-doped films, the improvement in hole delocalization is just a partial explanation for the increased conductivity. The second reason for such an improvement arises from the doping level. Mg has a limited solubility in Cr_2O_3: 6.6 at% cation substitution appears to be the maximum achievable, and any attempt to increase its concentration, either by varying the temperature or by increasing the Mg content in the target, resulted in phase separation. Conversely, Ni can be present in a considerably higher concentration (almost a factor of 3) without inducing phase separation. This high solubility is achieved by reducing the deposition temperature to a point where spurious phases are disfavored and the crystal quality of the Cr_2O_3 host-matrix is preserved. From a thermodynamic point of view, it would be expected that Mg and Ni should have comparable solubility, considering that DFT calculations show comparable formation energy. However, it has been shown that for some systems, non-equilibrium growth conditions can induce a considerable increase in the solubility of dopants, generating metastable compositions.[69–71] At very high doping concentrations, the Ni atoms are prone to aggregate.

This is clearly shown in the modulation of the Ni distribution in the Cr_2O_3 lamella, with layers of higher and lower Ni concentration that develop along the c-axis, further supported by the DFT calculations, which show that the system with all the dopant positioned close to each other has a lower energy than the system where the dopant atoms are homogeneously distributed.

6 Conclusion

A complementary experimental and theoretical investigation has been adopted to compare the potential of Mg- and Ni-doped Cr_2O_3 as p-type TCOs and to rationalise the observed higher conductivity of the Ni-doped samples over the Mg-doped. It was found that Ni is very effective p-type dopant in Cr_2O_3, capable of reaching conductivities of 28 S cm^{-1}. Both theoretical and experimental data has demonstrated that one of the major differences between the two dopants is the capability of Ni to contribute to the VB, contrary to Mg, whose electronic levels lie too deep. Ni contribution to the VB induces better delocalization of the formed holes and thus a lower effective mass. Formation energies and transition levels for a p-type defect whereby Ni/Mg replace a Cr atom in the structure are very similar in both cases and thus one could expect similar acceptor concentrations. However, it has been experimentally shown that Ni has a much higher solubility in Cr_2O_3 than Mg under certain non-equilibrium conditions, and its concentration is almost three times higher. The mixing of Ni states with the VB of the host material and the concomitant increase in the dopant concentration explain the improvement in the electrical properties of the material.

Authors contribution

E. A. designed and synthesized the material, performed structural, optical and electrical measurements; A. B. K., D. O. S., G. W. W. performed the DFT calculations; T. D. V. performed the XPS analysis; A. S., C. D., D. D., V. N. performed the TEM and EDX analysis; D. M., I. V. S. contributed to the electrical measurements.

Conflicts of interest

There are no conflicts to declare.

Acknowledgements

References

1 D. P. D. Ginley and H. Hosono, *Handbook of transparent conductors*, Springer, New York, 2010.
2 A. Klein, *J. Am. Ceram. Soc.*, 2013, **96**, 331–345.
3 J. Robertson, R. Gillen and S. J. Clark, *Thin Solid Films*, 2012, **520**, 3714–3720.
4 A. Stadleremail, *Materials*, 2012, **5**, 661–683.
5 S. Sallis, D. O. Scanlon, S. C. Chae, N. F. Quackenbush, D. A. Fischer, J. C. Woicik, J.-H. Guo, S. W. Cheong and L. F. J. Piper, *Appl. Phys. Lett.*, 2013, **103**, 042105.
6 D. O. Scanlon and G. W. Watson, *J. Phys. Chem. Lett.*, 2010, **1**, 3195–3199.
7 A. Walsh, J. L. F. Da Silva, S. H. Wei, C. Korber, A. Klein, L. F. J. Piper, A. DeMasi, K. E. Smith, G. Panaccione, P. Torelli, D. J. Payne, A. Bourlange and R. G. Egdell, *Phys. Rev. Lett.*, 2008, **100**, 167402.
8 N. F. Quackenbush, J. P. Allen, D. O. Scanlon, S. Sallis, J. A. Hewlett, A. S. Nandur, B. Chen, K. E. Smith, C. Weiland, D. A. Fischer, J. C. Woicik, B. E. White, G. W. Watson and L. F. J. Piper, *Chem. Mater.*, 2013, **25**, 3114–3123.
9 A. Zunger, *Appl. Phys. Lett.*, 2003, **83**, 57–59.
10 J. Robertson and S. J. Clark, *Phys. Rev. B: Condens. Matter Mater. Phys.*, 2011, **83**, 075205.
11 A. Walsh, J. Buckeridge, C. R. A. Catlow, A. J. Jackson, T. W. Keal, M. Miskufova, P. Sherwood, S. A. Shevlin, M. B. Watkins, S. M. Woodley and A. A. Sokol, *Chem. Mater.*, 2013, **25**, 2924–2926.
12 R. Nagarajan, A. D. Draeseke, A. W. Sleight and J. Tate, *J. Appl. Phys.*, 2001, **89**, 8022–8025.
13 R. Wei, X. Tang, L. Hu, Z. Hui, J. Yang, H. Luo, X. Luo, J. Dai, W. Song, Z. Yang, X. Zhu and Y. Sun, *Chem. Commun.*, 2014, **50**, 9697–9699.
14 K. H. L. Zhang, Y. Du, A. Papadogianni, O. Bierwagen, S. Sallis, L. F. J. Piper, M. E. Bowden, V. Shutthanandan, P. V. Sushko and S. A. Chambers, *Adv. Mater.*, 2015, **27**, 5191–5195.
15 M. O'Sullivan, P. Stamenov, J. Alaria, M. Venkatesan and J. M. D. Coey, *J. Phys.: Conf. Ser.*, 2010, **200**, 052021.
16 A. R. Nagaraja, N. H. Perry, T. O. Mason, Y. Tang, M. Grayson, T. R. Paudel, S. Lany and A. Zunger, *J. Am. Ceram. Soc.*, 2012, **95**, 269–274.
17 G. Hautier, A. Miglio, G. Ceder, G.-M. Rignanese and X. Gonze, *Nat. Commun.*, 2013, **4**, 2292.
18 B. J. Ingram, B. J. Harder, N. W. Hrabe, T. O. Mason and K. R. Poeppelmeier, *Chem. Mater.*, 2004, **16**, 5623–5629.
19 B. J. Ingram, T. O. Mason, R. Asahi, K. T. Park and A. J. Freeman, *Phys. Rev. B: Condens. Matter Mater. Phys.*, 2001, **64**, 155114.

20 G. J. Exarhos, C. F. Windisch Jr, K. F. Ferris and R. R. Owings, *Appl. Phys. A: Mater. Sci. Process.*, 2007, **89**, 9–18.

21 K. G. Godinho, B. J. Morgan, J. P. Allen, D. O. Scanlon and G. W. Watson, *J. Phys.: Condens. Matter*, 2011, **23**, 334201.

22 E. Fortunato, B. Raquel, B. Pedro, F. Vitor, P. Sang-Hee Ko, H. Chi-Sun and M. Rodrigo, *Appl. Phys. Lett.*, 2010, **97**, 052105.

23 H. Hosono, Y. Ogo, H. Yanagi and T. Kamiya, *Electrochem. Solid-State Lett.*, 2011, **14**, H13–H16.

24 H. Kawazoe, M. Yasukawa, H. Hyodo, M. Kurita, H. Yanagi and H. Hosono, *Nature*, 1997, **389**, 939–942.

25 R. Nagarajan, N. Duan, M. K. Jayaraj, J. Li, K. A. Vanaja, A. Yokochi, A. Draeseke, J. Tate and A. W. Sleight, *Int. J. Inorg. Mater.*, 2001, **3**, 265–270.

26 H. Kawazoe, H. Yanagi, K. Ueda and H. Hosono, *MRS Bull.*, 2000, **25**, 28–36.

27 A. Kudo, H. Yanagi, H. Hosono and H. Kawazoe, *Appl. Phys. Lett.*, 1998, **73**, 220–222.

28 K. G. Godinho, G. W. Watson, A. Walsh, A. J. H. Green, D. J. Payne, J. Harmer and R. G. Egdell, *J. Mater. Chem.*, 2008, **18**, 2798–2806.

29 X. Nie, S.-H. Wei and S. B. Zhang, *Phys. Rev. Lett.*, 2002, **88**, 066405.

30 M.-S. Miao, S. Yarbro, P. T. Barton and R. Seshadri, *Phys. Rev. B: Condens. Matter Mater. Phys.*, 2014, **89**, 045306.

31 P. T. Barton, R. Seshadri, A. Knoller and M. J. Rosseinsky, *J. Phys.: Condens. Matter*, 2012, **24**, 016002.

32 H. Hiramatsu, K. Ueda, H. Ohta, M. Hirano, T. Kamiya and H. Hosono, *Appl. Phys. Lett.*, 2003, **82**, 1048–1050.

33 H. Hiramatsu, K. Ueda, H. Ohta, M. Hirano, M. Kikuchi, H. Yanagi, T. Kamiya and H. Hosono, *Appl. Phys. Lett.*, 2007, **91**, 012104.

34 K. Ueda, S. Inoue, S. Hirose, H. Kawazoe and H. Hosono, *Appl. Phys. Lett.*, 2000, **77**, 2701–2703.

35 D. O. Scanlon, J. Buckeridge, C. R. A. Catlow and G. W. Watson, *J. Mater. Chem. C*, 2014, **2**, 3429–3438.

36 M. Dekkers, G. Rijnders and D. H. A. Blank, *Appl. Phys. Lett.*, 2007, **90**, 021903.

37 J. D. Perkins, T. R. Paudel, A. Zakutayev, P. F. Ndione, P. A. Parilla, D. L. Young, S. Lany, D. S. Ginley, A. Zunger, N. H. Perry, Y. Tang, M. Grayson, T. O. Mason, J. S. Bettinger, Y. Shi and M. F. Toney, *Phys. Rev. B: Condens. Matter Mater. Phys.*, 2011, **84**, 205207.

38 A. R. Nagaraja, K. H. Stone, M. F. Toney, H. Peng, S. Lany and T. O. Mason, *Chem. Mater.*, 2014, **26**, 4598–4604.

39 D. O. Scanlon and G. W. Watson, *Phys. Chem. Chem. Phys.*, 2011, **13**, 9667–9675.

40 J. Im, G. Trimarchi, H. Peng, A. J. Freeman, V. Cloet, A. Raw and K. R. Poeppelmeier, *J. Chem. Phys.*, 2013, **138**, 194703.

41 V.-A. Ha, F. Ricci, G.-M. Rignanese and G. Hautier, *J. Mater. Chem. C*, 2017, **5**, 5772–5779.

42 E. Arca, K. Fleischer and I. V. Shvets, *Appl. Phys. Lett.*, 2011, **99**, 111910.

43 E. Arca, K. Fleischer, S. A. Krasnikov and I. Shvets, *J. Phys. Chem. C*, 2013, **117**, 21901–21907.

44 F. Lebreau, M. M. Islam, B. Diawara and P. Marcus, *J. Phys. Chem. C*, 2014, **118**, 18133–18145.

45 E. Arca, M. A. McInerney and I. V. Shvets, *J. Phys.: Condens. Matter*, 2016, **28**, 224004.

46 A. B. Kehoe, E. Arca, D. O. Scanlon, I. V. Shvets and G. W. Watson, *J. Phys.: Condens. Matter*, 2016, **28**, 125501.

47 J. J. Carey and M. Nolan, *J. Mater. Chem. A*, 2017, **5**, 15613–15630.

48 A. Atkinson, M. R. Levy, S. Roche and R. A. Rudkin, *Solid State Ionics*, 2006, **177**, 1767–1770.

49 A. Holt and P. Kofstad, *Solid State Ionics*, 1999, **117**, 21–25.

50 F. Maldonado, C. Novillo and A. Stashans, *Chem. Phys.*, 2012, **393**, 148–152.

51 A. N. Blacklocks, A. Atkinson, R. J. Packer, S. L. P. Savin and A. V. Chadwick, *Solid State Ionics*, 2006, **177**, 2939–2944.

52 A. Holt and P. Kofstad, *Solid State Ionics*, 1997, **100**, 201–209.

53 N. Uekawa and K. Kaneko, *J. Phys. Chem.*, 1996, **100**, 4193–4198.

54 G. M. Crosbie, G. J. Tennenhouse, R. P. Tischer and H. S. Wroblowa, *J. Am. Ceram. Soc.*, 1984, **67**, 498–503.

55 G. Kresse and J. Hafner, *Phys. Rev. B: Condens. Matter Mater. Phys.*, 1994, **49**, 14251–14271.

56 G. Kresse and J. Furthmüller, *Comput. Mater. Sci.*, 1996, **6**, 15–50.

57 G. Kresse and J. Furthmüller, *Phys. Rev. B: Condens. Matter Mater. Phys.*, 1996, **54**, 11169–11186.

58 J. P. Perdew, K. Burke and M. Ernzerhof, *Phys. Rev. Lett.*, 1996, **77**, 3865–3868.

59 S. L. Dudarev, G. A. Botton, S. Y. Savrasov, C. J. Humphreys and A. P. Sutton, *Phys. Rev. B: Condens. Matter Mater. Phys.*, 1998, **57**, 1505–1509.

60 A. M. Ferrari, C. Pisani, F. Cinquini, L. Giordano and G. Pacchioni, *J. Chem. Phys.*, 2007, **127**, 174711.

61 A. B. Kehoe, D. O. Scanlon and G. W. Watson, *Chem. Mater.*, 2011, **23**, 4464–4468.

62 C. Freysoldt, J. Neugebauer and C. G. V. de Walle, *Phys. Rev. Lett.*, 2009, **102**, 016402.

63 P. H. Fang and W. S. Brower, *Phys. Rev.*, 1963, **129**, 1561.

64 M. W. Cho, A. Setiawan, H. J. Ko, S. K. Hong and T. Yao, *Semicond. Sci. Technol.*, 2005, **20**, S13–S21.

65 O. Durand, A. Letoublon, D. J. Rogers and F. Hosseini Teherani, *Thin Solid Films*, 2011, **519**, 6369–6373.

66 R. D. Shannon, *Acta Crystallogr., Sect. A: Cryst. Phys., Diffr., Theor. Gen. Crystallogr.*, 1976, **32**, 751–767.

67 A. Subramaniyan, J. D. Perkins, R. P. O'Hayre, D. S. Ginley, S. Lany and A. Zakutayev, *J. Mater. Sci.*, 2014, **50**, 1350–1357.

68 R. G. Gordon, *MRS Bull.*, 2000, **25**, 52–57.

69 A. Zakutayev, V. Stevanovic and S. Lany, *Appl. Phys. Lett.*, 2015, **106**, 123903.

70 A. K. Sharma, J. Narayan, J. F. Muth, C. W. Teng, C. Jin, A. Kvit, R. M. Kolbas and O. W. Holland, *Appl. Phys. Lett.*, 1999, **75**, 3327–3329.

71 H. Peng, P. F. Ndione, D. S. Ginley, A. Zakutayev and S. Lany, *Phys. Rev. X*, 2015, **5**, 021016.

12618 | *J. Mater. Chem. C*, 2017, **5**, 12610–12618

This journal is © The Royal Society of Chemistry 2017